

Two-step Carbothermal Welding to Access Atomically Dispersed Pd₁ on 3D Zirconia Nanonet for Direct Indole Synthesis

Yafei Zhao,^{1,†} Huang Zhou,^{1,†} Wenxing Chen,^{3,†} Yujing Tong,¹ Chao Zhao,¹ Yue Lin,¹ Zheng Jiang,⁵ Qingwei Zhang,¹ Zhenggang Xue,¹ Weng-Chon Cheong,² Benjin Jin,¹ Fangyao Zhou,¹ Wenyu Wang,¹ Min Chen,¹ Xun Hong,¹ Juncai Dong,⁴ Shiqiang Wei,⁶ Yadong Li², Yuen Wu^{1,*}

¹Department of Chemistry, Hefei National Laboratory for Physical Sciences at the Microscale, iChEM (Collaborative Innovation Center of Chemistry for Energy Materials), University of Science and Technology of China, Hefei 230026, China;

²Department of Chemistry, Tsinghua University, Beijing 100084, PR. China;

³Beijing Key Laboratory of Construction Tailorable Advanced Functional Materials and Green Applications, School of Materials Science and Engineering, Beijing Institute of Technology, Beijing 100081, P. R. China.

⁴Institute of Physics, Chinese Academy of Sciences, Beijing 100190, P. R. China.

⁵Shanghai Synchrotron Radiation Facilities, Shanghai Institute of Applied Physics, Shanghai 201800, P. R. China.

⁶National Synchrotron Radiation Laboratory, University of Science and Technology of China, Hefei 230026, China;

Table of contents

1. Experiment detail
2. Supplementary Figures and Tables
3. References

Section1. Experiment detail

Materials

All chemicals were used as received without further purification. 2-amino terephthalic acid ($\text{H}_2\text{BDC-NH}_2$), zirconium chloride (ZrCl_4), hydrofluoric acid solution (HF 40%) were purchased by Shanghai Chemical Reagents. Palladium chloride, acetic acid, 2-(2-nitrophenyl)acetaldehyde, commercial ZrO_2 and DMF were purchased from Aladdin Company. Deionized water was used throughout this study.

Preparation of UiO-66-NH₂

In a typical procedure,^[1-3] a mixture of ZrCl_4 (315 mg) and $\text{H}_2\text{BDC-NH}_2$ (245 mg) was dissolved in 300 mL DMF containing 40 mL of HAc in a 500 mL round-bottom flask. The mixture was treated with ultrasound for 0.5 h to form a homogeneous transparent solution. Then, the mixture was heated at 120 °C for 3 h before it cooled to room temperature. The as-obtained products were centrifuged at 7000 rpm for 3 min and washed with methanol and DMF (1/4 v/v) for three times. Finally, the as-prepared UiO-66-NH₂ was dried under vacuum at 65 °C for further use.

Preparation of PdCl₂/UiO-66-NH₂

First, the Pd precursor (PdCl_2) was adsorbed through the unsaturated dangling -NH₂ groups by wet impregnation. Briefly, a mixed precursor of ZrCl_4 (315 mg) and $\text{PdCl}_2/\text{H}_2\text{BDC-NH}_2$ (5.6 mg/245 mg) was dissolved in 300 mL of DMF containing 36 mL of glacial acetic acid in a 500 mL round-bottom flask. The mixture was treated with ultrasound for 0.5 h to form a homogeneous transparent solution. Then, the mixture was heated at 120 °C for 3 h before it cooled to room temperature. The as-obtained products were centrifuged at 7000 rpm for 3 min and washed with methanol and DMF (1/4 v/v) for three times. Finally, the as-prepared $\text{PdCl}_2/\text{UiO-66-NH}_2$ was dried in vacuum at 65 °C for overnight.

Preparation of Pd₁@NC/ZrO₂

The as-prepared $\text{PdCl}_2/\text{UiO-66-NH}_2$ (100 mg) was placed in a tube furnace and then heated to 900 °C at a heating rate of 5 °C/min under a flowing argon atmosphere. It was followed by another 3 h treatment at 900 °C under argon atmosphere. After cooling to room temperature,

the black powder was collected for future use.

Preparation of Pd₁@ZrO₂ and U-ZrO₂

The first, the as-prepared PdCl₂/UiO-66-NH₂ (100 mg) was placed in a tube furnace and then heated to 900 °C for 3 h at a heating rate of 5 °C/min under a flowing argon atmosphere and then air atmosphere (600 °C) for 3 min to yield Pd₁@ZrO₂. The synthetic procedure of U-ZrO₂ was same as that of Pd₁@ZrO₂, except for using UiO-66-NH₂ instead of PdCl₂/UiO-66-NH₂.

Preparation of Pd₁@NC

The black powder of Pd₁@CN/ZrO₂ was dispersed in 15 mL of H₂O containing 0.1 mol HF for 2 h, and then centrifuged at 11000 rpm for 5 min. Subsequently, the resultant product was washed with methanol and H₂O (v/v 1:4) for three times and dried under vacuum at 65 °C for further use.

Characterization

Powder X-ray diffraction (XRD) measurements were recorded on a Rigaku Miniflex-600 operated at 40 kV voltage and 15 mA current using a Cu K α radiation ($\lambda=0.15406$ nm) at a step width of 8°/min. TEM images were recorded on a Hitachi-7650 worked at 100 kV. The high-resolution TEM, HAADF-STEM images and the corresponding Electron energy-loss spectroscopy were recorded on a FEI Tecnai G2 F20 S-Twin high-resolution transmission electron microscope worked at 200 kV and a JEOL JEM-ARM200F TEM/STEM with a spherical aberration corrector worked at 300 kV. Through-focal HAADF series were acquired at nanometer intervals, with the first image under-focused (beyond the beam exit surface) and the final image over-focused (before the beam entrance surface). The images were then manually aligned to remove the sample drift effects. Elemental analysis of Pd in the solid samples was detected by inductively coupled plasma atomic emission spectrometry (Optima 7300 DV). Hard XAFS measurement and data analysis: XAFS spectra at the Pd and Fe K-edge were recorded at the XAS station (BL14W1) of the Shanghai Synchrotron Radiation Facility (SSRF), China. The Pd and Fe K-edge XANES data were recorded in a fluorescence mode. The storage ring worked at the energy of 3.5 GeV. The hard X-ray was monochromatized with Si (111) double-crystals. The acquired EXAFS data were extracted and processed according to the standard procedures using the ATHENA module implemented in the IFEFFIT software packages. The k³-weighted EXAFS spectra were obtained by subtracting the post-edge background from the overall absorption and then normalizing with respect to the edge-jump step. Subsequently, k³-weighted $\chi(k)$ data in the k-space were Fourier

transformed to real (R) space using a hanning windows ($d_k=3.00-12.173 \text{ \AA}^{-1}$) to separate the EXAFS contributions from different coordination shells. To obtain the quantitative structural parameters around central atoms, least-squares curve parameter fitting was performed using the ARTEMIS module of IFEFFIT software packages. The following EXAFS equation was used.

$$\chi(k) = \sum_j \frac{N_j S_o^2 F_j(k)}{k R_j^2} \exp[-2 k^2 \sigma_j^2] \exp\left[-\frac{2 R_j}{\lambda(k)}\right] \sin[2k R_j + \phi_j(k)]$$

S_o^2 is the amplitude reduction factor, $F_j(k)$ is the effective curved-wave back scattering amplitude, N_j is the number of neighbors in the j th atomic shell, R_j is the distance between the X-ray absorbing central atom and the atoms in the j th atomic shell (back scatterer), λ is the mean free path in \AA , $\phi_j(k)$ is the phase shift (including the phase shift for each shell and the total central atom phase shift), σ_j is the Debye-Waller parameter of the j th atomic shell (variation of distances around the average R_j). The functions $F_j(k)$, λ and $\phi_j(k)$ were calculated with the ab initio code FEFF8.2.

Catalytic evaluation

The reactions were operated with the 25 mL Schlenk glass vessel tubes under 0.1 MPa H_2 atmosphere. In a typical experiment, the reaction solutions of 0.005 mmol of 2-(2-Nitrophenyl)acetaldehyde, 2 mL of DMF and different catalysts ($Pd_1@ZrO_2$, U- ZrO_2 , $Pd_1@NC$) with a weight ratio of 1:1000 (catalyst: reactant) were loaded into the reactor. Then, the reactor was heated to the 80 °C temperature and the stirring speed fixed to 600 rpm to ensure that the diffusion effect was eliminated. Mesitylene (1 mmol) used as the internal standard was added in the beginning of the reaction. The product was identified by the gas chromatography–mass spectrometry (GC-MS, Thermo Fisher Scientific-TXQ Quntum XLS, column-TG-WAXMS, 30 m \times 0.25 mm \times 0.25 μ m), and was quantitatively analyzed by GC (Shimadzu, GC-2010 Plus), equipped with FID and a (30 m \times 0.25 mm \times 0.25 μ m) KB-WAX capillary column (Kromat Corporation, USA) using mesitylene as an internal standard.

Section2. Supporting Figures and Tables

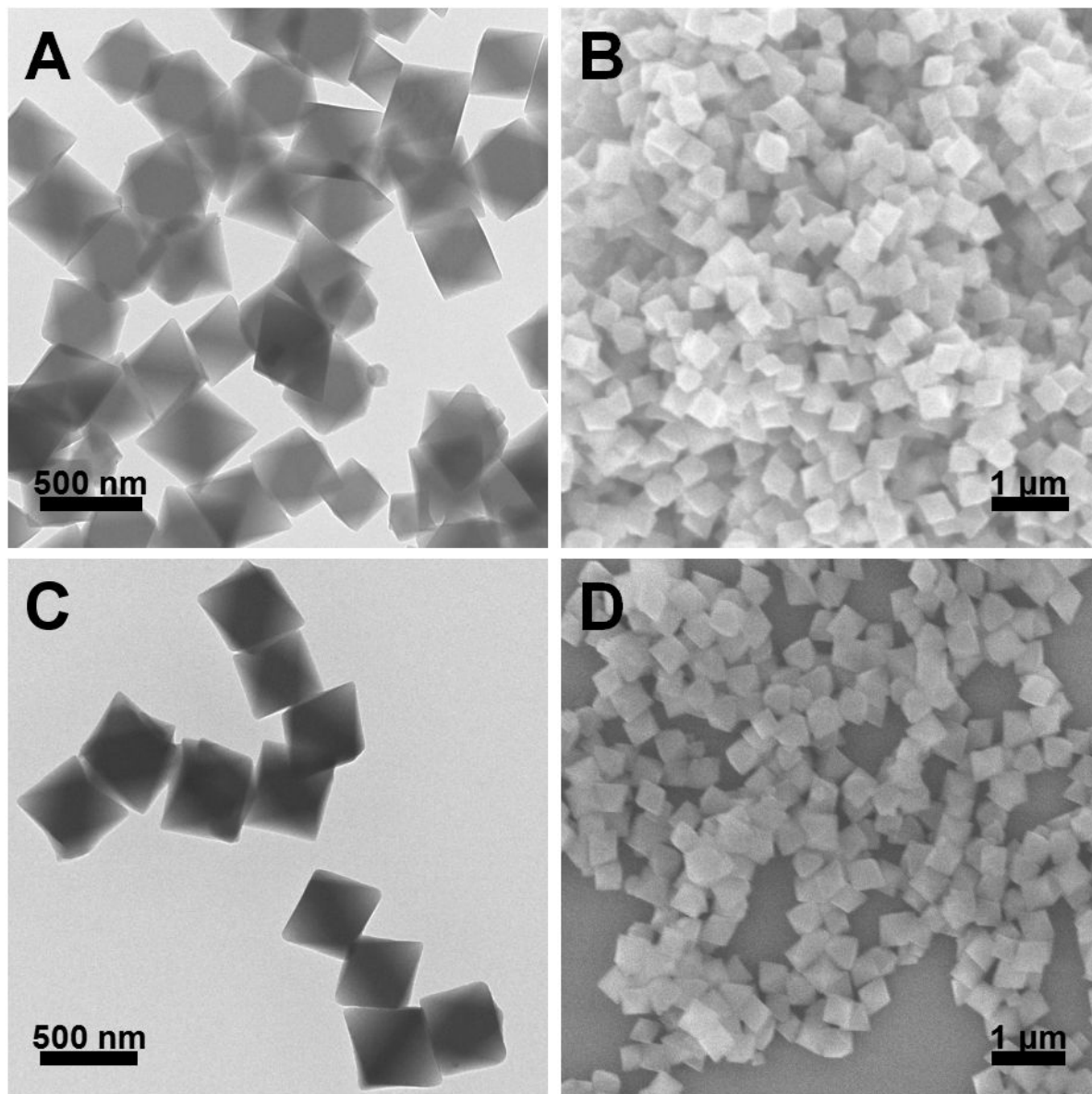


Fig. S1. TEM images of UiO-66-NH₂ (A) and PdCl₂/UiO-66-NH₂ (C). SEM images of UiO-66-NH₂ (B) and PdCl₂/UiO-66-NH₂ (D).

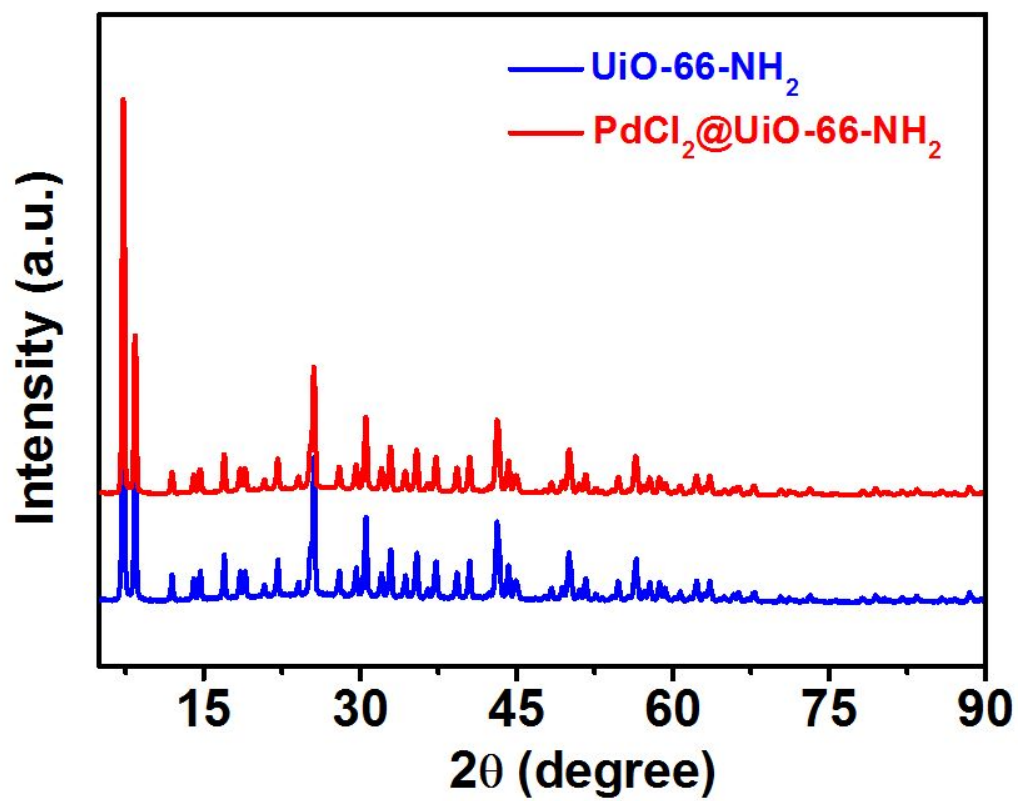


Fig. S2. XRD patterns of UiO-66-NH₂ and PdCl₂@UiO-66-NH₂.

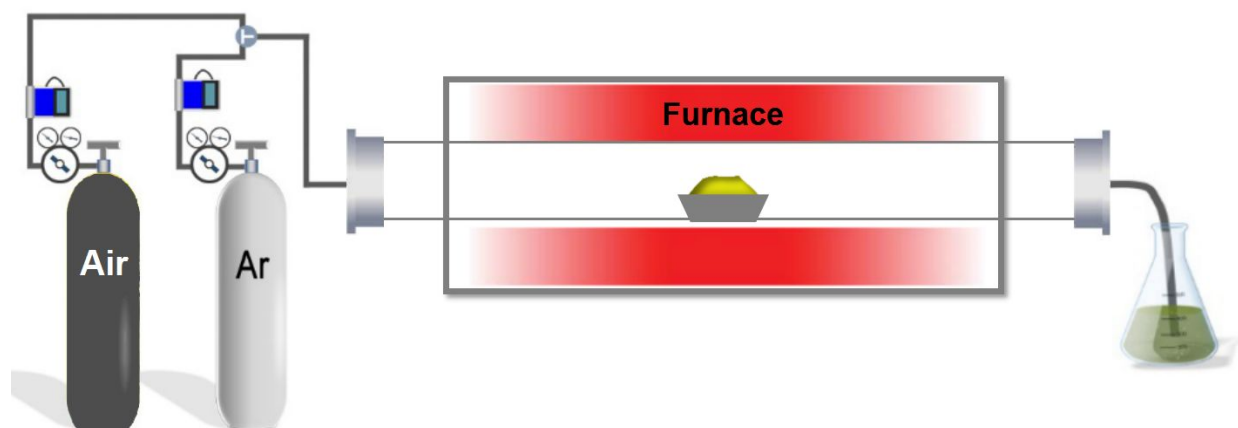


Fig. S3. Schematic illustration of a home-built tube furnace.

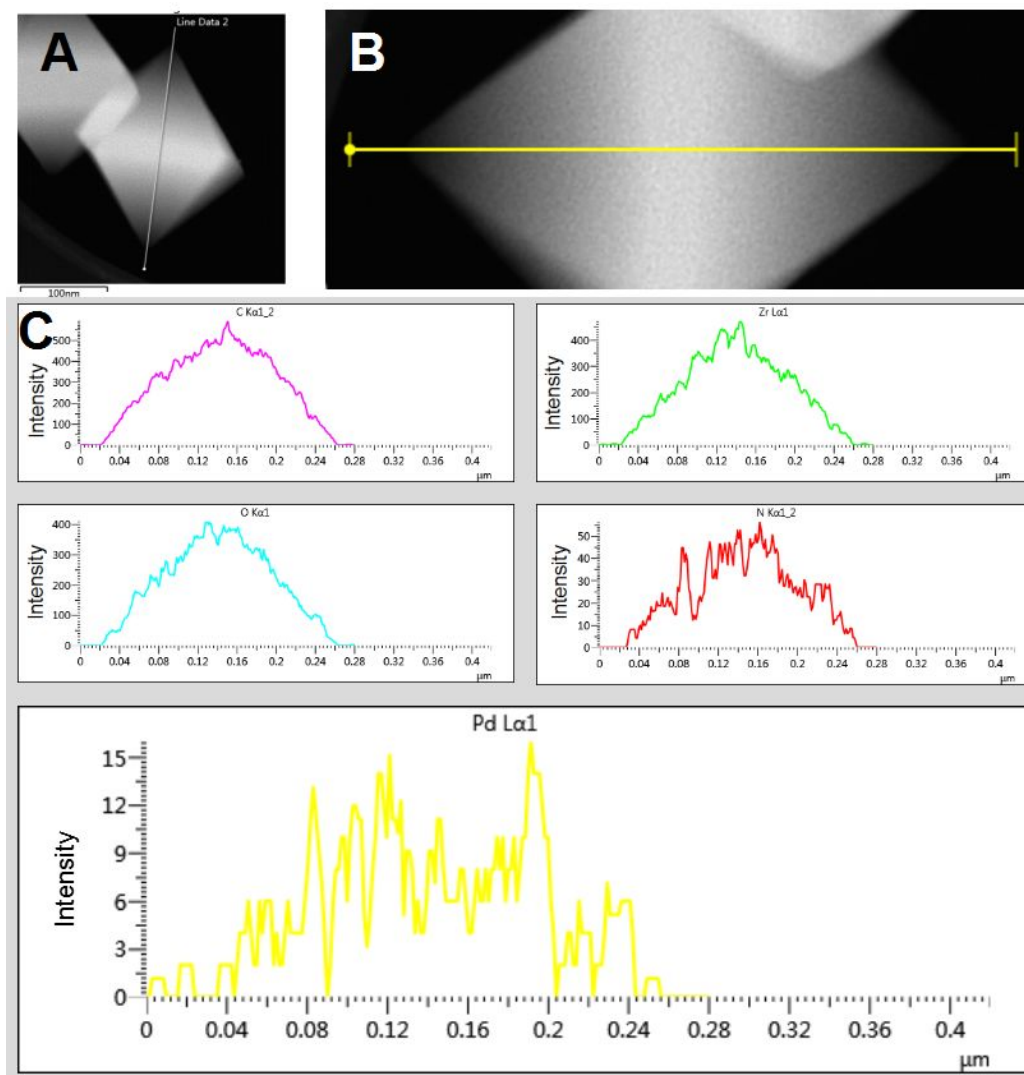


Fig. S4. Dark field image of $\text{Pd}_1\text{@NC/ZrO}_2$ (A and B) and EDX spectroscopy line-scan profile, indicating C, Zr, O, N, Pd were homogeneously distributed in whole MOF skeletons (C).

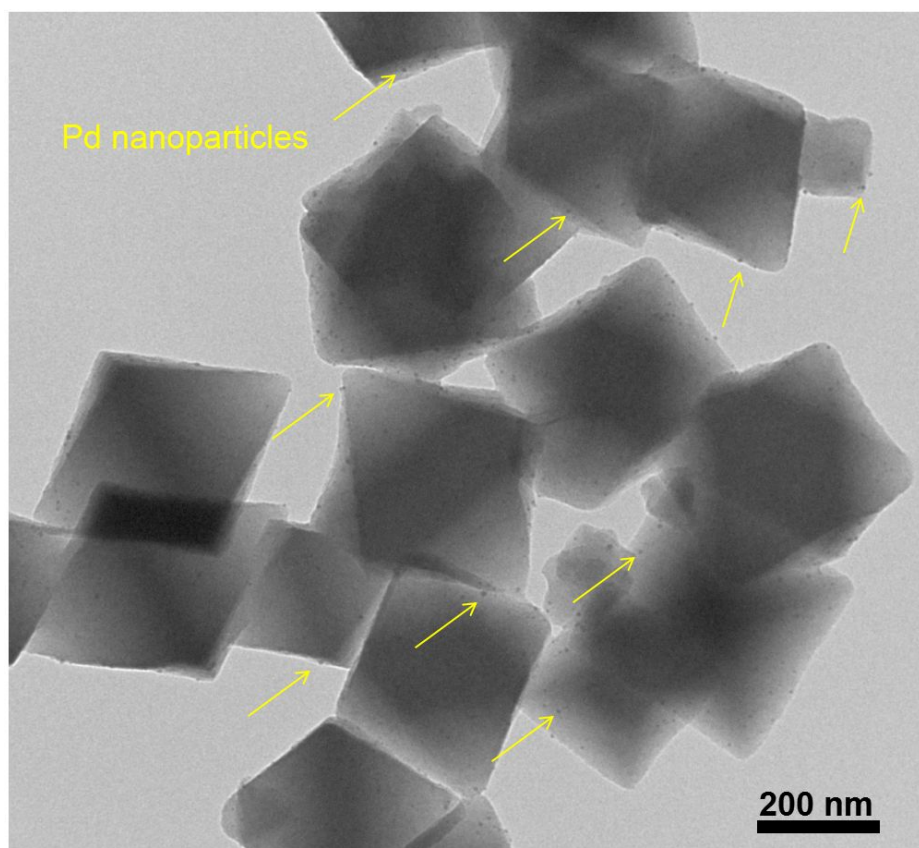


Fig. S5. The representative TEM image of Pd nanoparticles anchored onto the terephthalic-acid-derived carbon support through the pyrolysis of PdCl₂@UiO-66 (PdCl₂:H₂BDC:ZrCl₄ = 5.6 mg : 227 mg: 315 mg). Without the assistance of -NH₂ groups, a large proportion of Pd atoms would aggregate at high temperature, resulting in the formation of Pd nanoparticles.

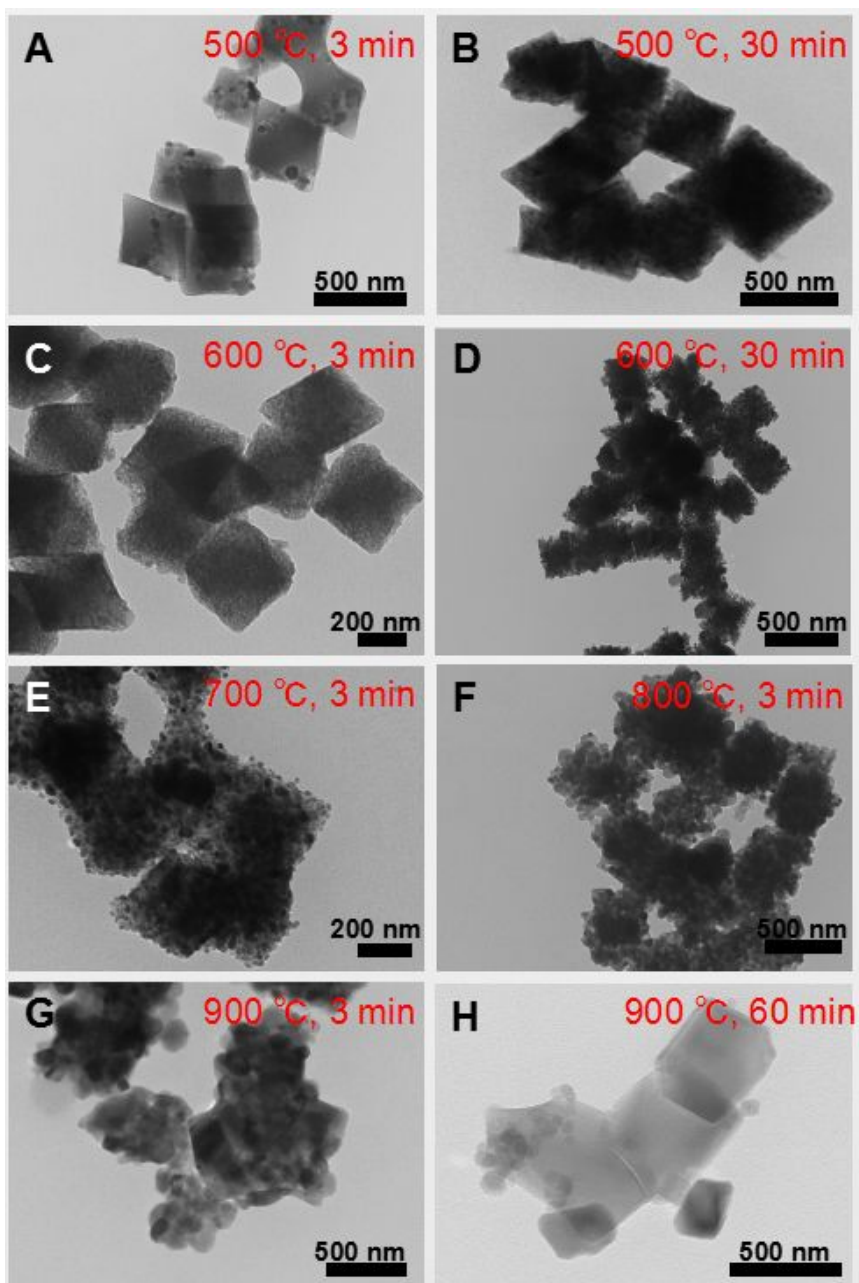


Fig. S6. NC removing process of $\text{Pd}_1\text{@NC/ZrO}_2$ was treated under various temperature in air. The optimal temperature was give to 600 °C (3 min).

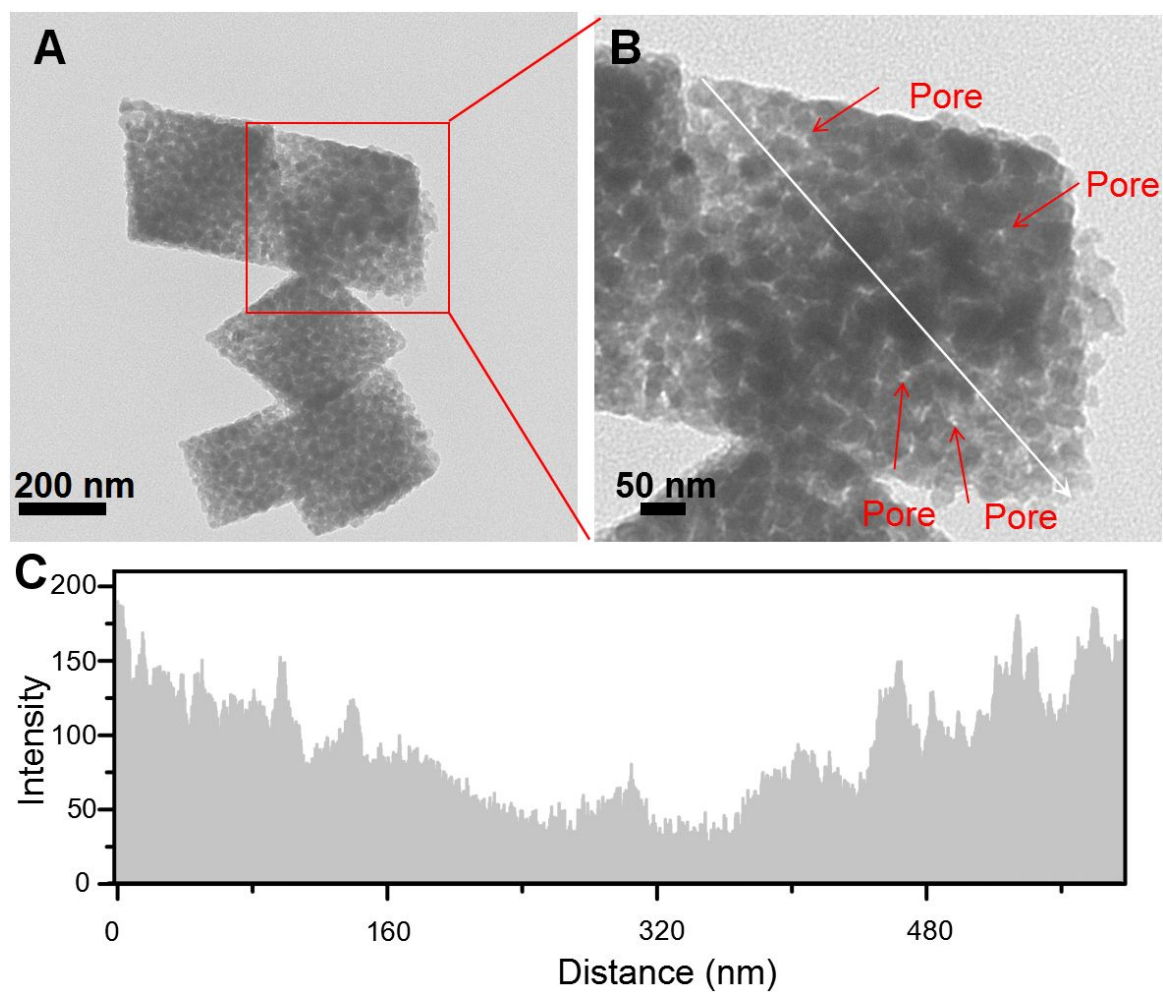


Fig. S7. TEM image (A) and its magnified image (B) of Pd₁@ZrO₂. (C) Corresponding intensity profiles obtained from the white line in (B), indicating the surface of ZrO₂ skeletons was more fluctuant and porous.

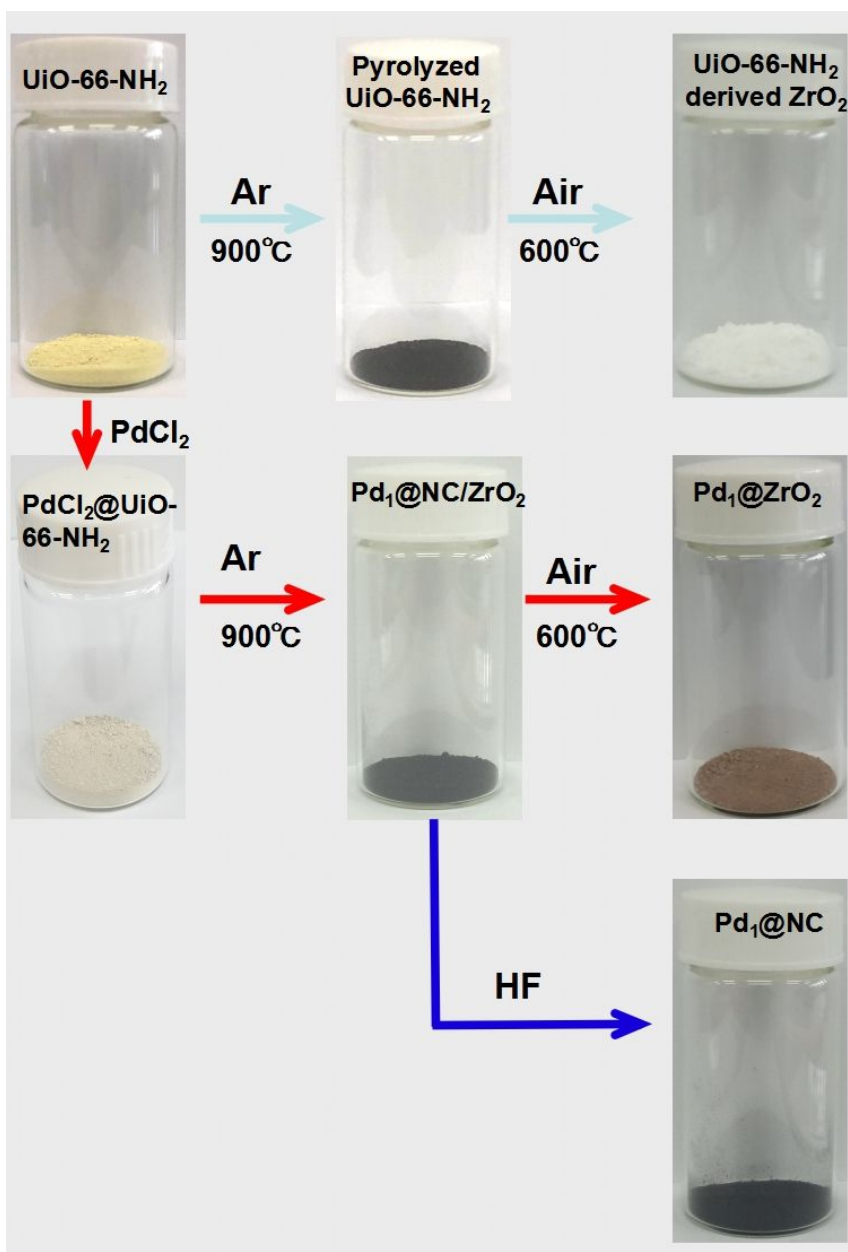


Fig. S8. The color evolution during the preparation of UiO-66-NH₂ derived ZrO₂, Pd₁@NC/ZrO₂, Pd₁@ZrO₂, and Pd₁@NC.

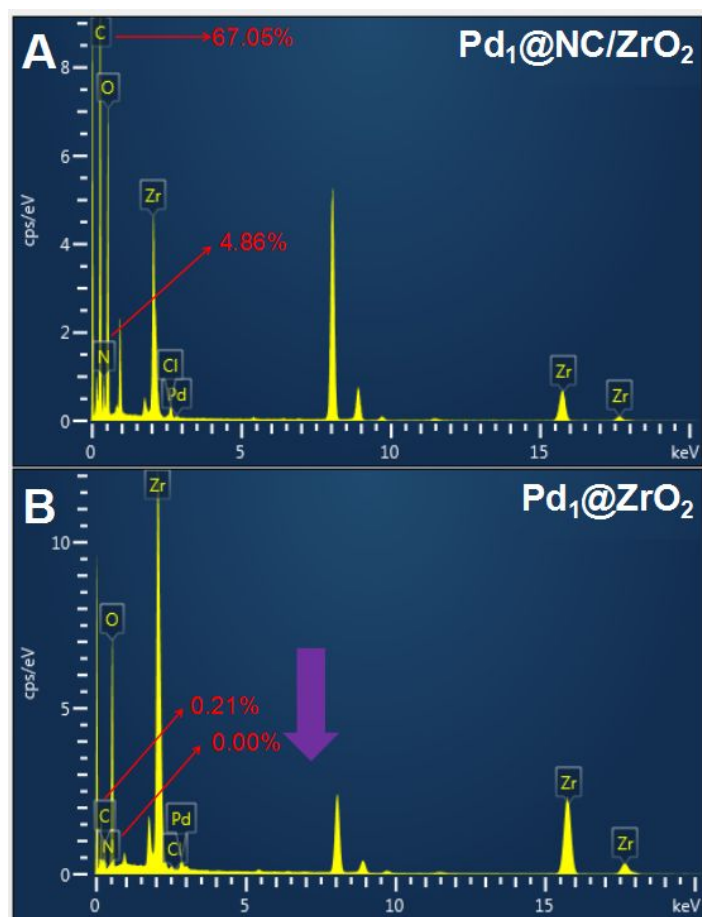


Fig. S9. EDS spectra of $\text{Pd}_1@\text{NC}/\text{ZrO}_2$ (Figure 2F) and $\text{Pd}_1@\text{ZrO}_2$ (Figure 2J).

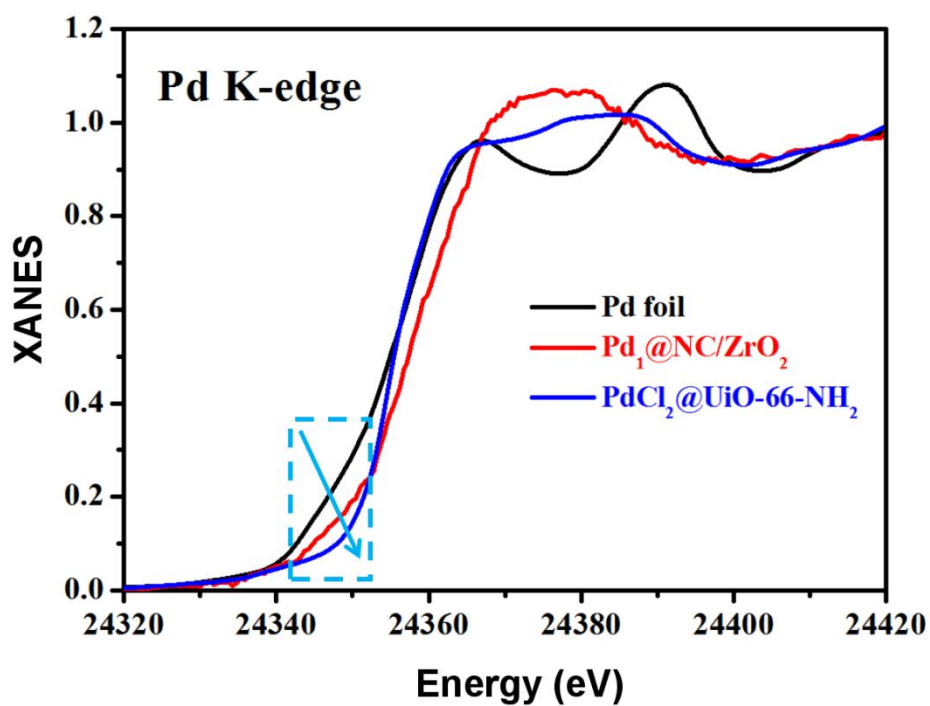


Fig. S10. XANES spectra of PdCl₂@UiO-66-NH₂, Pd₁@NC/ZrO₂, and Pd foil.

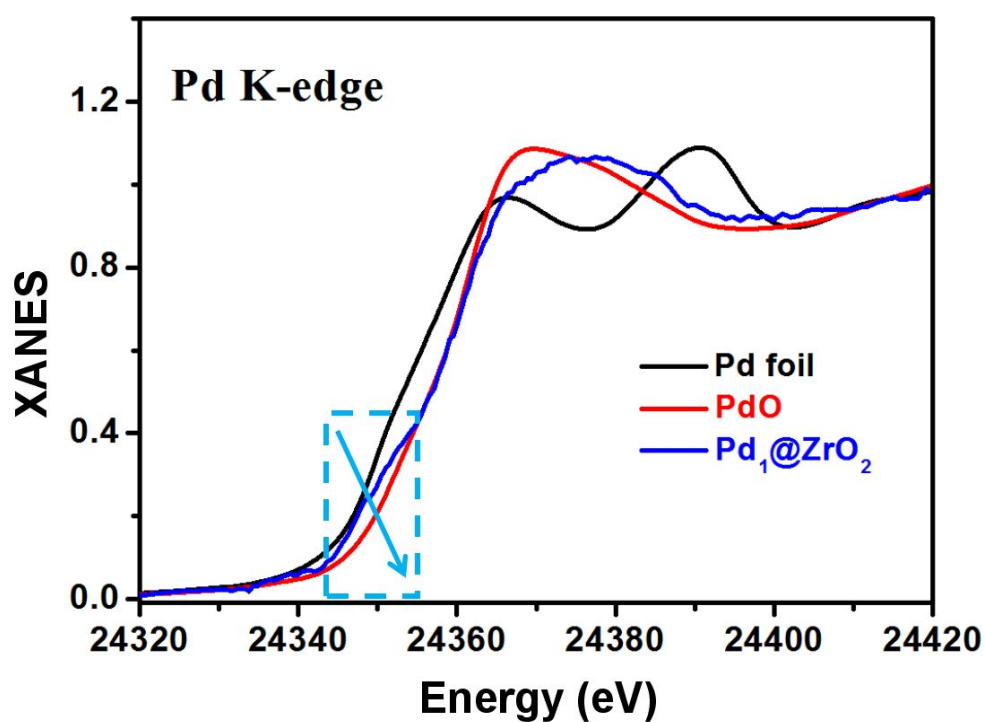


Fig. S11. XANES spectra of Pd₁@ZrO₂, PdO, and Pd foil.

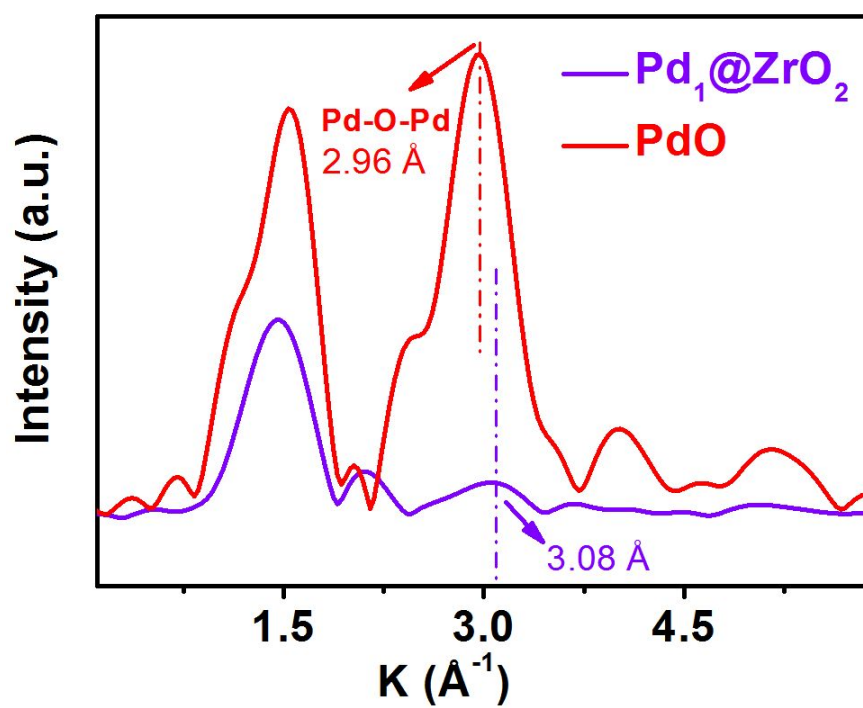


Fig. S12. FT-EXAFS of Pd₁@ZrO₂ and PdO.

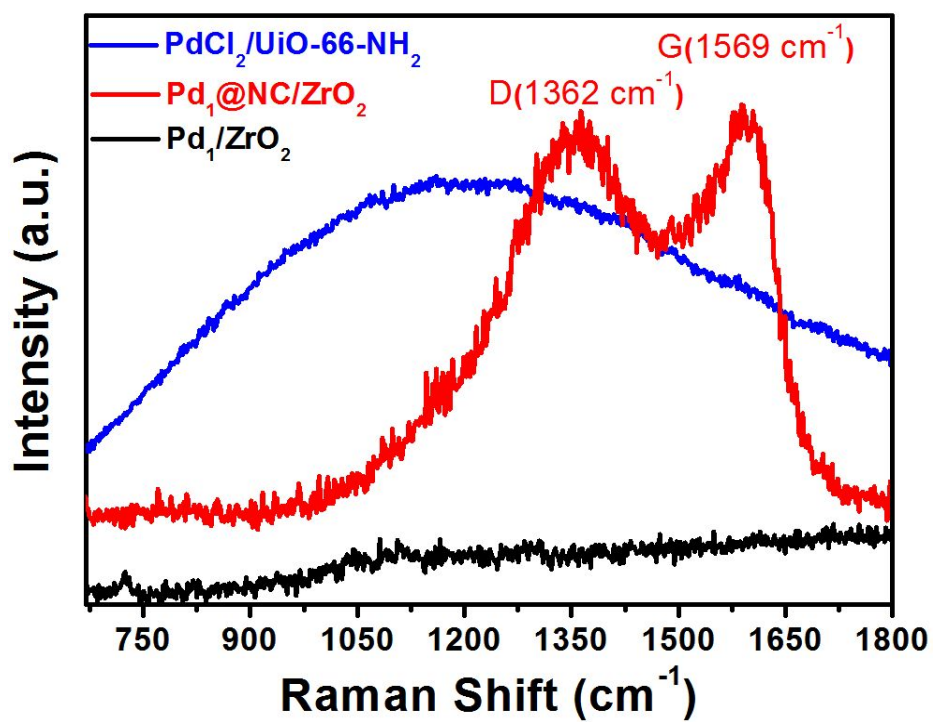


Fig. S13. Raman spectra of PdCl₂@UiO-66-NH₂, Pd₁@NC/ZrO₂, and Pd₁@ZrO₂.

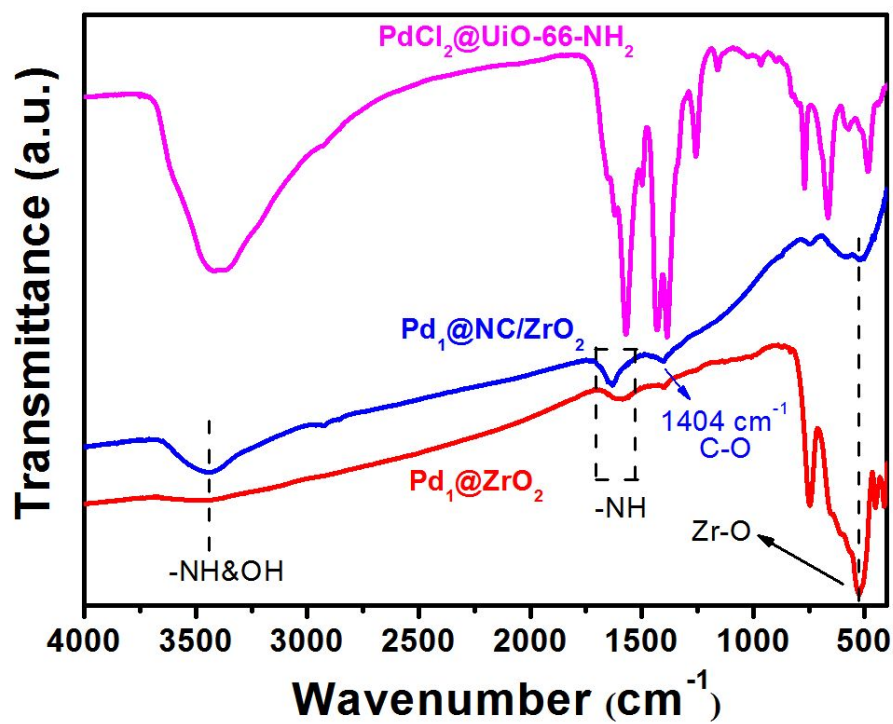


Fig. S14. FT-IR spectra of $\text{PdCl}_2@\text{UiO-66-NH}_2$, $\text{Pd}_1@\text{NC/ZrO}_2$, and $\text{Pd}_1@\text{ZrO}_2$. The peak located at 522 cm^{-1} was assigned to Zr-O absorption band.^[4]

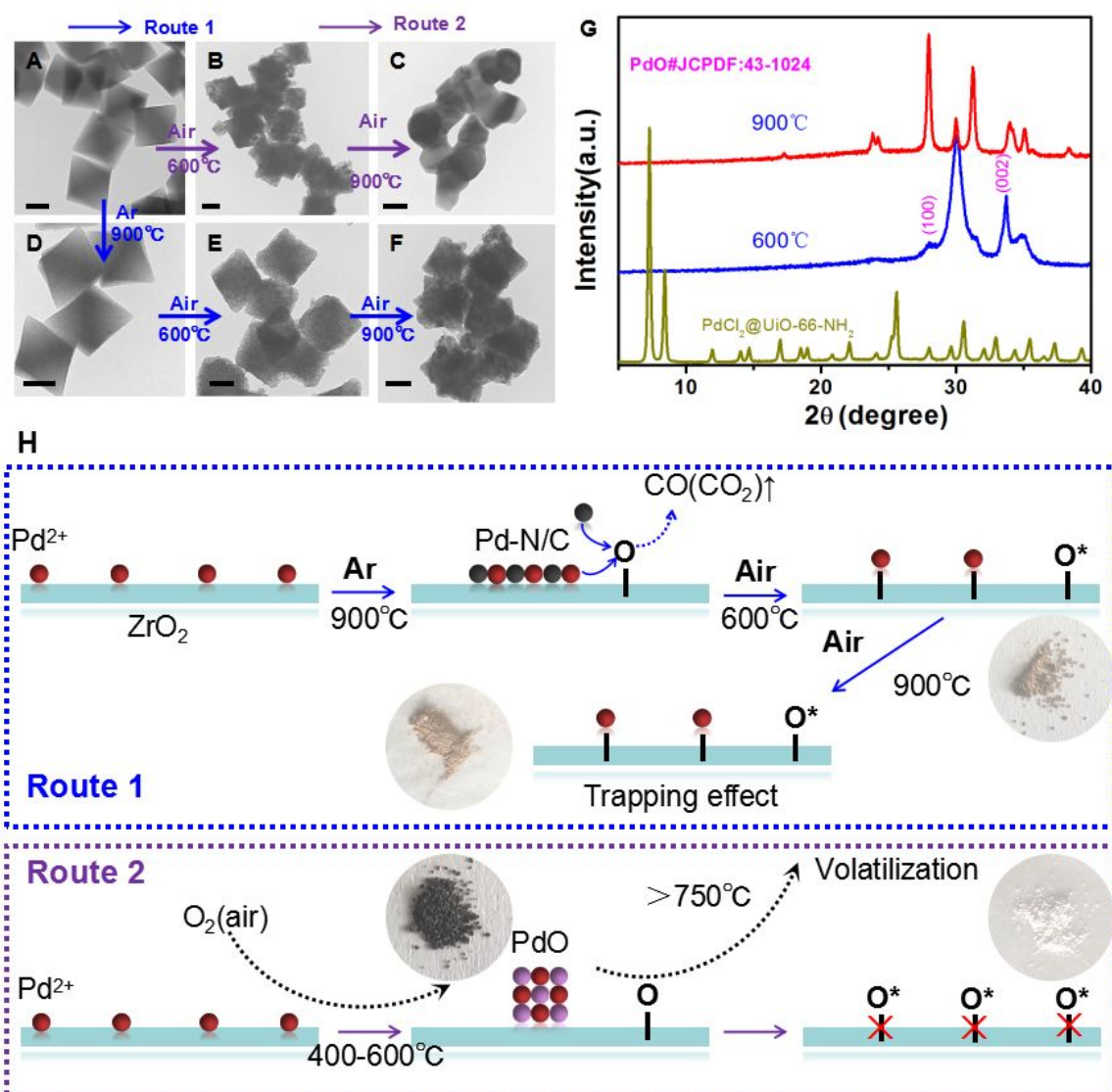


Fig. S15. (A-F) TEM images of $\text{PdCl}_2@\text{UiO-66-NH}_2$ under various heat treatment. (Insets are the TEM images. The scale bars, 200 nm). (G) XRD patterns of $\text{PdCl}_2@\text{UiO-66-NH}_2$ under pyrolysis in air. (H) The pyrolysis paths for the $\text{PdCl}_2@\text{UiO-66-NH}_2$.

The $\text{PdCl}_2@\text{UiO-66-NH}_2$ (Route 2) was first pyrolyzed at 600 °C (3 min) in air. The adsorbent Pd^{2+} was bonded with O_2 (derived from air) to yield PdO and 2-aminoterephthalate ligands were directly gasified in a lower temperature range (400-600 °C). No obvious chemical attachment between PdO and ZrO_2 nodes was produced. At 900 °C in air, the surface PdO was evaporated to form volatile species ($\approx 750^\circ\text{C}$) to escape from ZrO_2 support. Correspondingly, the color of the samples evolved from brown to white and the characteristic peaks [(100) and (002)] of PdO entirely dispersed. After two-step carbothermal welding, the as-obtained $\text{Pd}_1@\text{ZrO}_2$ was further pyrolyzed at 900 °C (3 min) in air (Route 1). The colors of the samples were not obviously changed, indicating Pd species was surface-bound by a strong trapping effect between Pd and ZrO_2 .

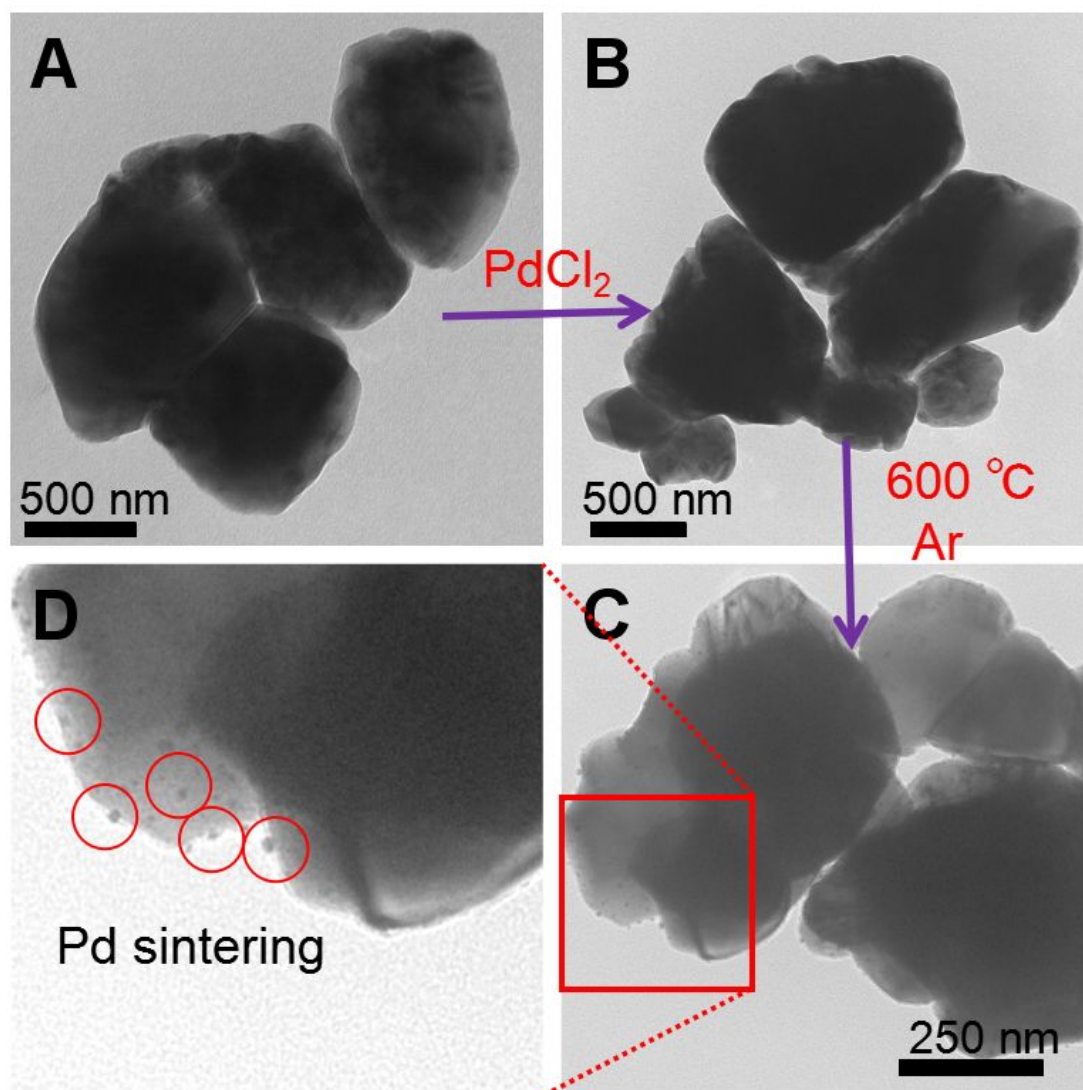


Fig. S16. TEM images of (A) commercial ZrO₂, (B) PdCl₂/commercial ZrO₂, (C) Pd nanoparticles/commercial ZrO₂, and (D) magnified TEM images.

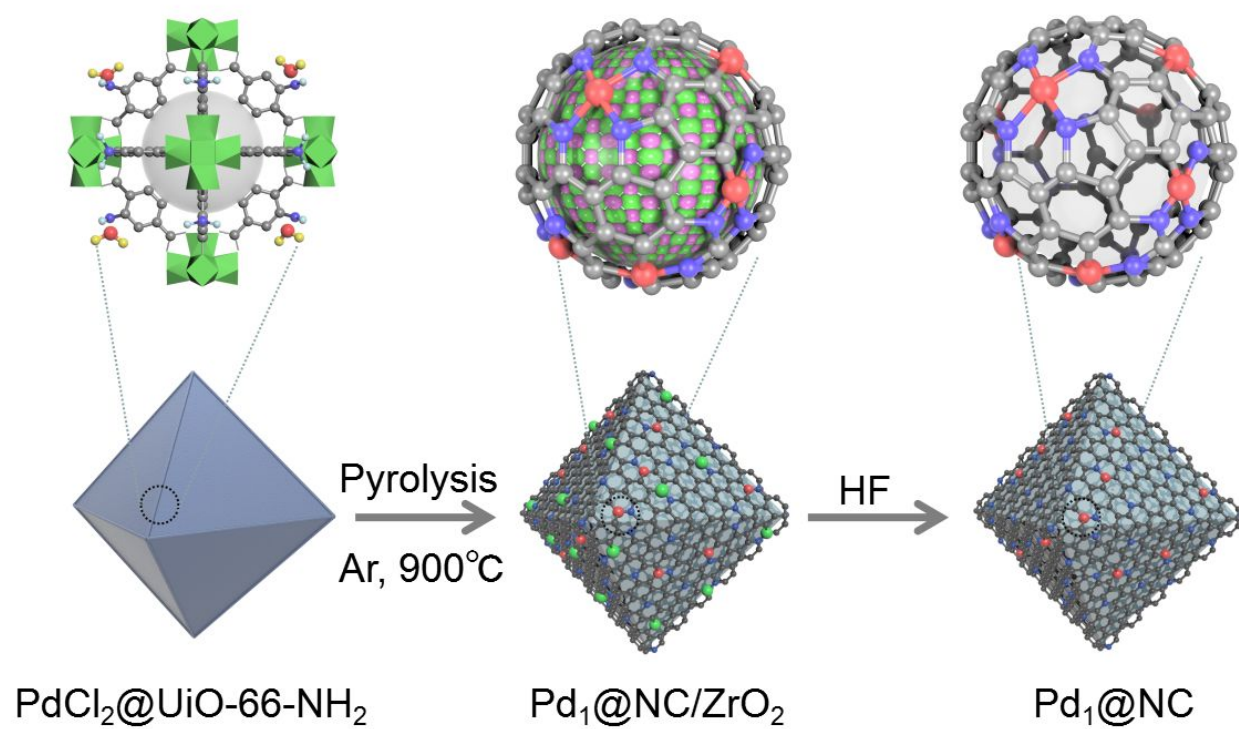


Fig. S17. Scheme of the formation of Pd₁@NC.

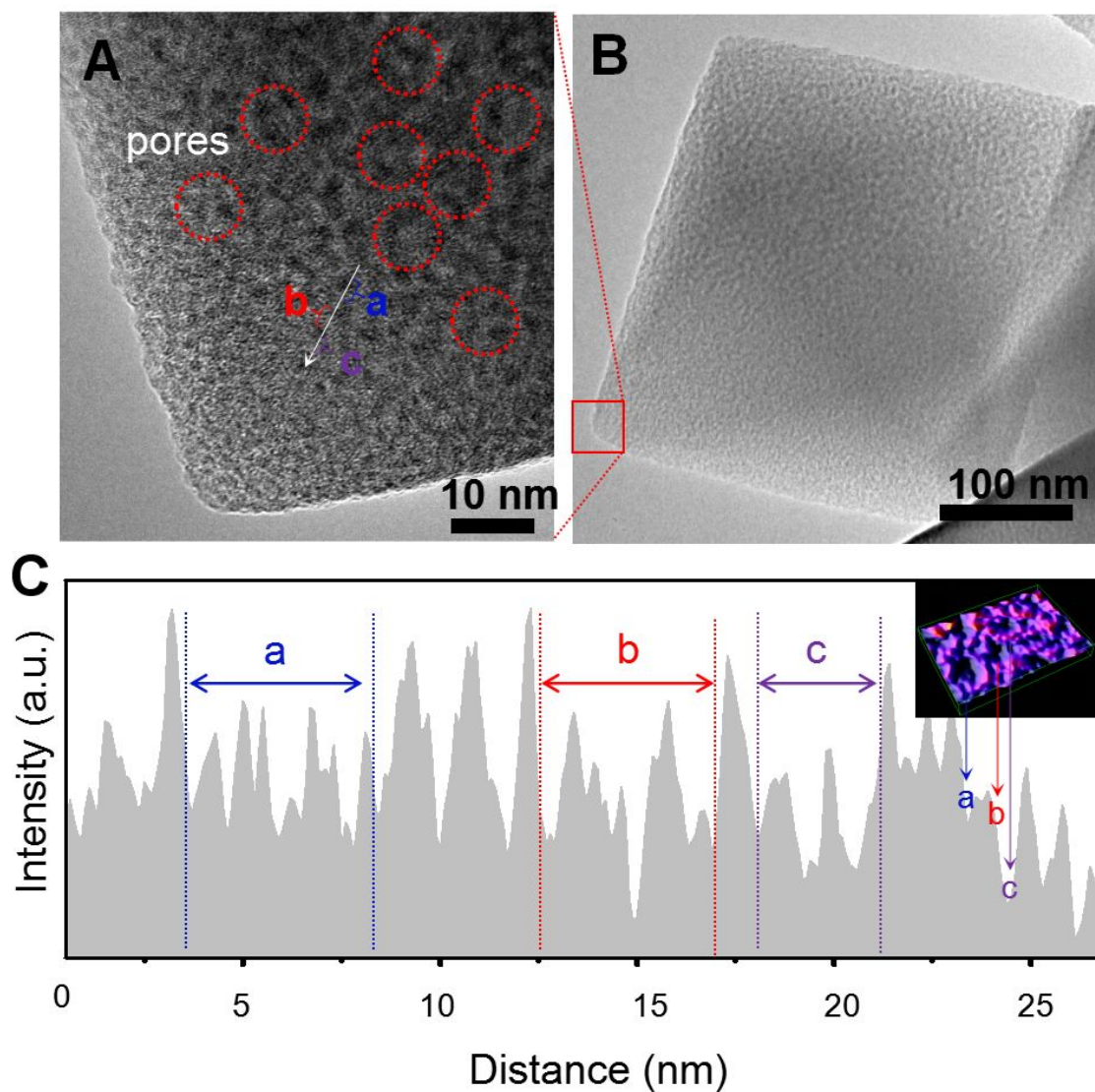


Fig. S18. HRTEM image (A) and TEM image (B) of Pd₁@NC after being removed ZrO₂ via HF etching. (C) Corresponding intensity profiles obtained from the white line in (B), indicating the linker-derived NC skeletons retained its initial shape and the pore derived from ultrasmall ZrO₂ was exposed. The insets was 3D atom-overlapping gaussian-function fitting mapping.

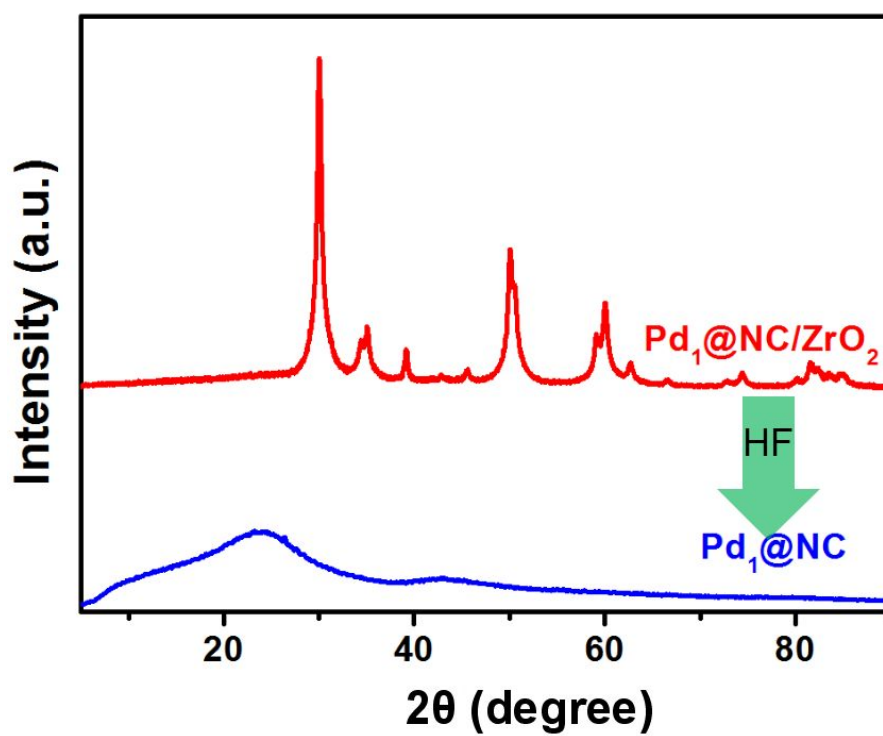


Fig. S19. XRD patterns of $\text{Pd}_1\text{@NC/ZrO}_2$ before and after HF treatment.

As revealed by the XRD pattern, the addition of HF solution could readily etch the inert ZrO_2 nanoparticles,^[5] resulting in the formation of Pd single sites ($\text{Pd}_1\text{@NC}$) anchored on an amorphous N-doped carbon skeletons.

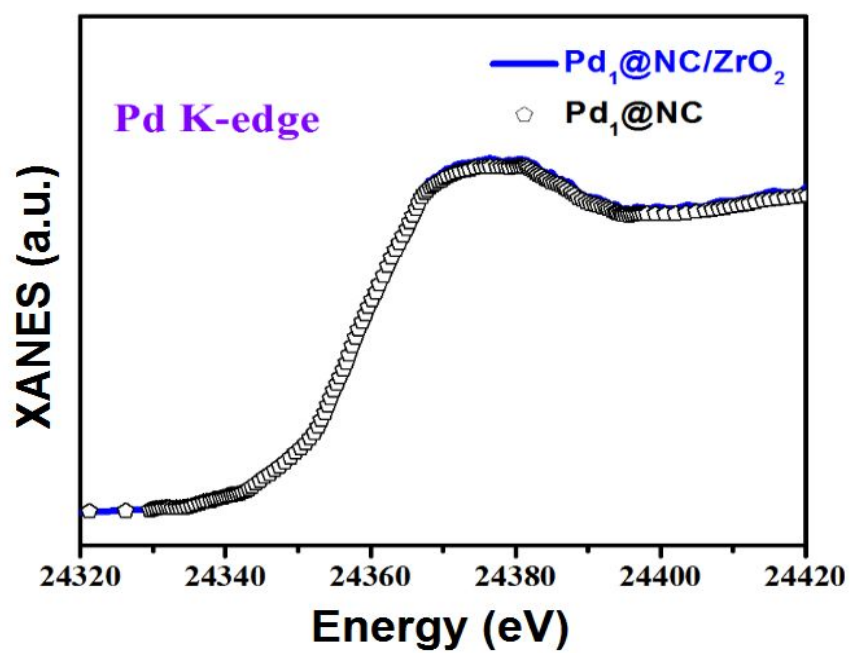


Fig. S20. XANES of $\text{Pd}_1\text{@NC/ZrO}_2$ before and after HF treatment.

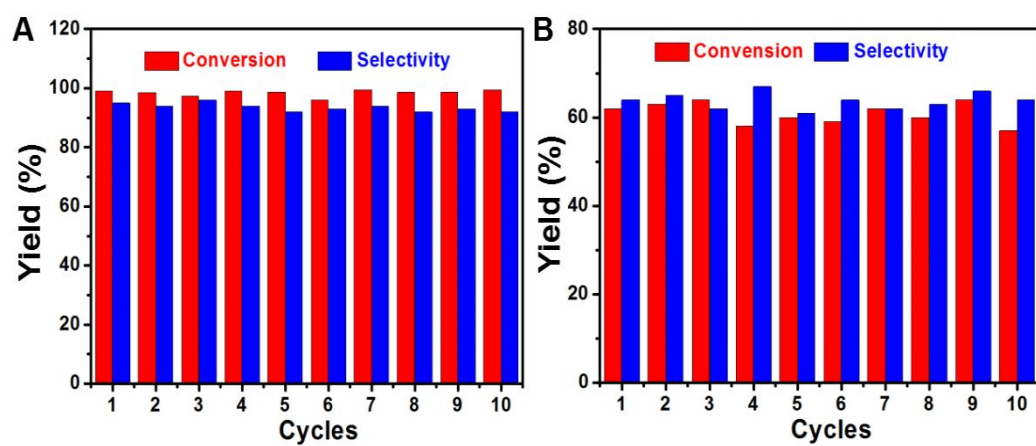


Fig. S21. The recyclability of (A) Pd₁@ZrO₂ and (B) Pd₁@NC.

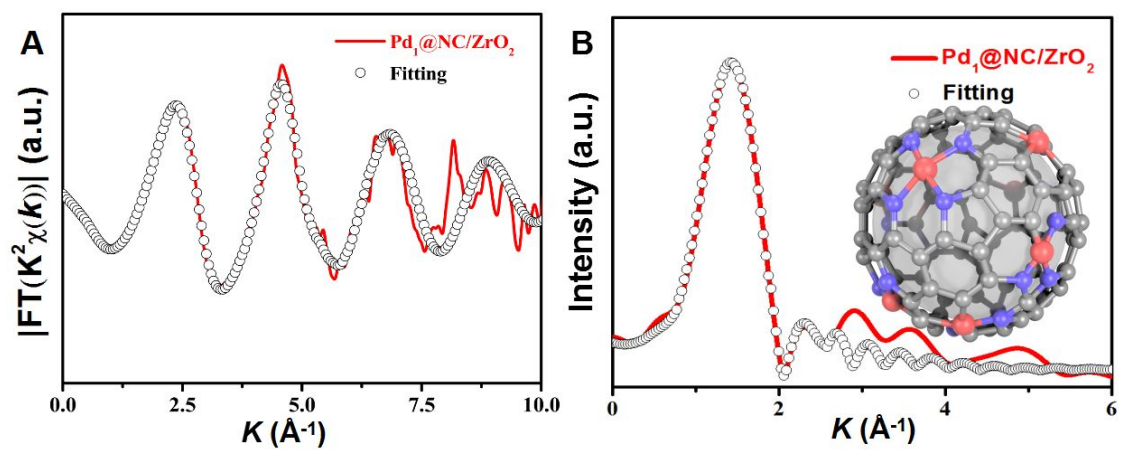


Fig. S22. The corresponding (A) inverse and (B) R space FT-EXAFS fitting curves for $\text{Pd}_1@NC/ZrO_2$. Inset is the proposed $\text{Pd}-N_xC_{4-x}$ ($0 \leq x \leq 4$) architectures.

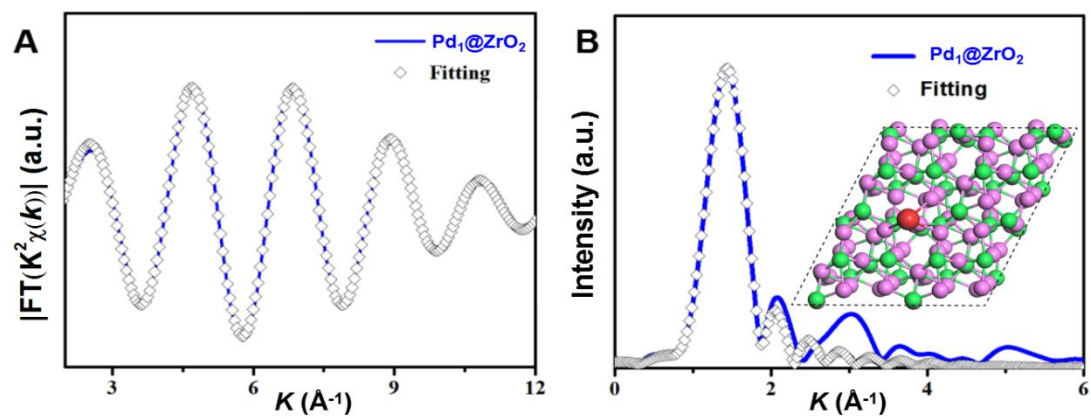


Fig. S23. The corresponding (A) inverse and (B) R space FT-EXAFS fitting curves for $\text{Pd}_1@ZrO_2$. Inset is the proposed Pd-O_3 architectures.

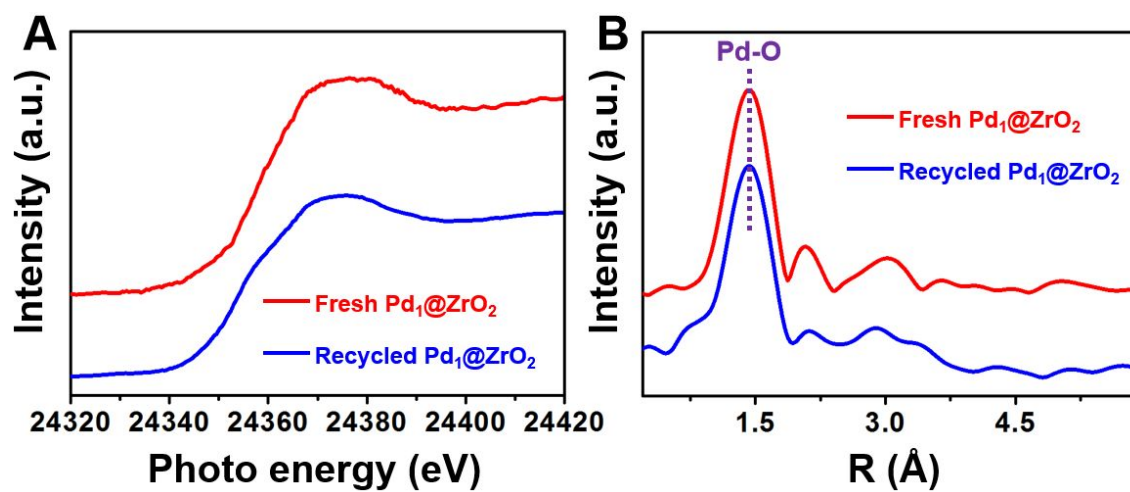


Fig. S24. XANES (A) and FT-EXAFS (B) analysis of $\text{Pd}_1@\text{ZrO}_2$ after reaction.

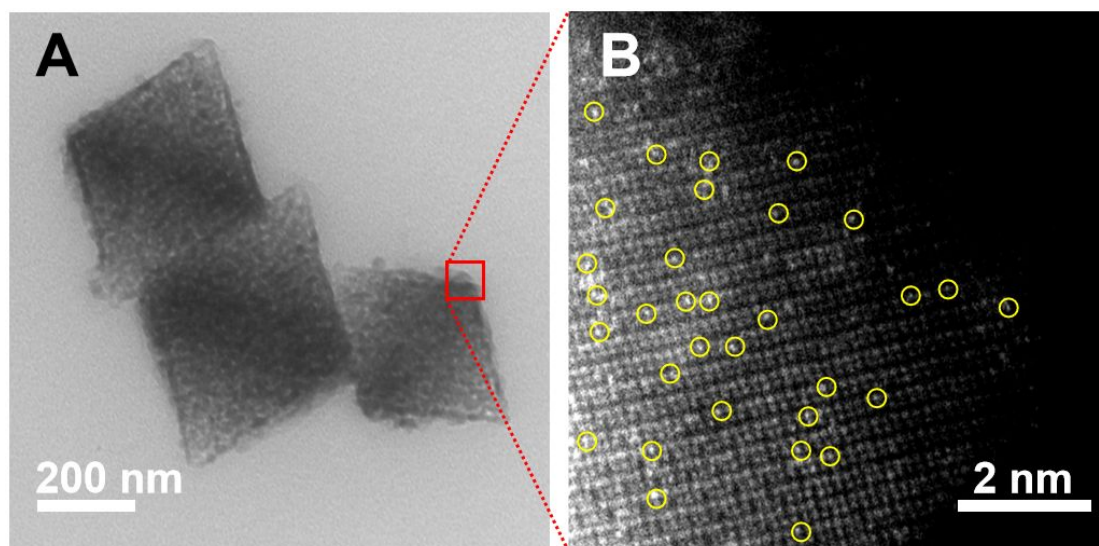


Fig. S25. AC HAADF-STEM images of $\text{Pd}_1@\text{ZrO}_2$ after reaction.

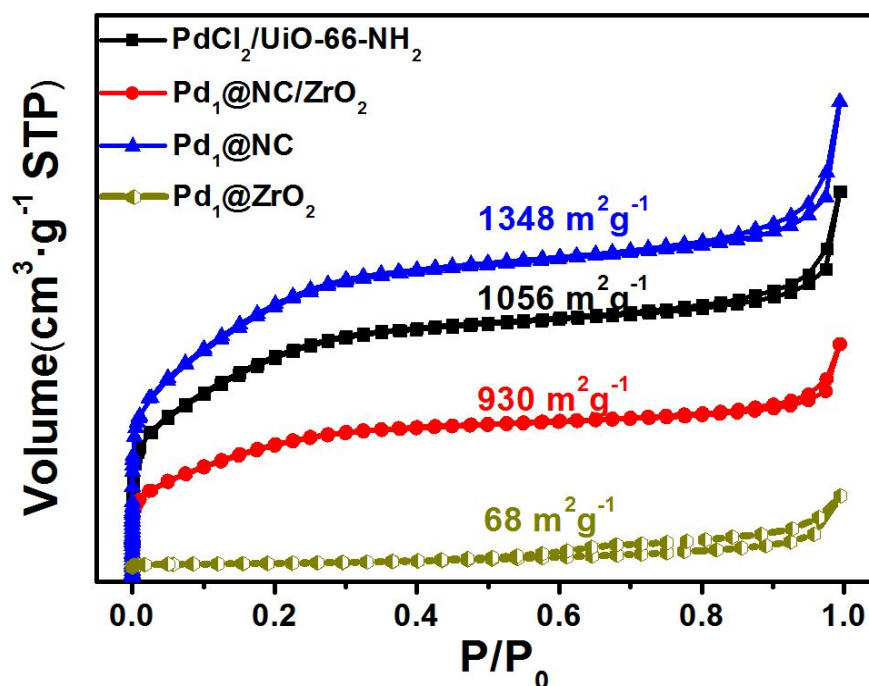


Fig. S26. N₂ adsorption and desorption isotherm for PdCl₂@UiO-66-NH₂, Pd₁@NC/ZrO₂, Pd₁@NC and Pd₁@ZrO₂. The BET specific surface areas of the as-prepared samples were obtained by recording nitrogen adsorption-desorption isotherms at 77 K. The sample were degassed under 300 °C for 360 min (Instrument Model: Autosorb iQ S/N:14716042101). The etching treatment of Pd₁@NC/ZrO₂ thought HF increased the BET surface areas from 930 to 1348 m²g⁻¹, indicating the NC skeletons were intact. The NC etching process leads to an obviously decrease of the BET surface areas, further verifying that NC was successful being removed.

Table S1. Inductively coupled plasma optical emission spectrometry (ICP-OES) measurements.

<i>Sample</i>	<i>The content of Pd (wt%)</i>
Commercial ZrO ₂	0
PdCl ₂ @UiO-66-NH ₂	0.12
Pd ₁ @NC/ZrO ₂	0.32
Pd ₁ @NC	0.78
Pd ₁ @ZrO ₂	0.44

Table S2. EXAFS parameters of Pd₁@NC/ZrO₂, Pd₁@ZrO₂, and references.

<i>Sample</i>	<i>Path</i>	<i>N</i>	<i>R</i> (Å)	σ^2 (10 ⁻³ Å ²)	ΔE_0 (eV)	<i>R-factor</i>
Pd ₁ @NC/ZrO ₂	Pd-N/C	4	2.00 ± 0.01	3.7	-2.21	0.004
Pd ₁ @ZrO ₂	Pd-O	3	2.00 ± 0.02	6.1	-1.7	0.0054
Pd foil	Pd-Pd	12.0*	2.74	5.4	3.9	0.001

N is the coordination number; R is interatomic distance (the bond length between central atoms and surrounding coordination atoms); σ^2 is Debye-Waller factor (a measure of thermal and static disorder in absorber-scatterer distances); ΔE_0 is edge-energy shift (the difference between the zero kinetic energy value of the sample and that of the theoretical model). *R* factor is used to value the goodness of the fitting. *This value was fixed during EXAFS fitting, based on the known structure of Pd. Error bounds that characterize the structural parameters obtained by EXAFS spectroscopy were estimated as $N \pm 20\%$; $R \pm 1\%$; $\sigma^2 \pm 20\%$; $\Delta E_0 \pm 20\%$.

References

- [1] Cavka, J. H.; Jakobsen, S.; Olsbye, U.; Guillou, N.; Lamberti, C.; Bordiga, S.; Lillerud, K. P. A new zirconium inorganic building brick forming metal organic frameworks with exceptional stability. *J. Am. Chem. Soc.* **2008**, 130, 13850–13851.
- [2] Wang, X.; Chen, W.; Zhang, L.; Yao, T.; Liu, W.; Lin, Y.; Ju, H.; Dong, J.; Zheng, L.; Yan, W. Uncoordinated amine groups of metal–organic frameworks to anchor single Ru sites as chemoselective catalysts toward the hydrogenation of quinoline. *J. Am. Chem. Soc.* **2017**, 139, 9419–9422.
- [3] Kandiah, M.; Nilsen, M. H.; Usseglio, S.; Jakobsen, S.; Olsbye, U.; Tilset, M.; Larabi, C.; Quadrelli, E. A.; Bonino, F.; Lillerud, K. P. Synthesis and stability of tagged UiO-66 Zr-MOFs. *Chem. Mater.* **2010**, 22, 6632–6640.
- [4] Gnanamoorthi, K.; Balakrishnan, M.; Kumar, E. Ranjith.; Prakash, T.; Mariappan, R. Structural, Optical and Gas Sensing Performance of Pure and Doped ZrO₂. *J. Adv. Phys.* **2017**, 6, 508–513.
- [5] Yang, J.; Zhang, F.; Wang, X.; He, D.; Wu, G.; Yang, Q.; Hong, X.; Wu, Y.; Li, Y. Porous molybdenum phosphide nano-octahedrons derived from confined phosphorization in UiO-66 for efficient hydrogen evolution. *Angew. Chem. Int. Ed.* **2016**, 55, 12854–12858.
- [6] Wei, S. J.; Li, A.; Liu, J. C.; Li, Z.; Chen, W. X.; Gong, Y.; Zhang, Q. H.; Cheong, W. C.; Wang, Y.; Zheng, L. R.; Xiao, H.; Chen, C.; Wang, D. S.; Peng, Q.; Gu, L.; Han, X. D.; Li, J.; Li, Y. D. Direct observation of noble metal nanoparticles transforming to thermally stable single atoms. *Nat. Nanotechnol.* **2018**, 13, 856–861.